

Far-field sheaths due to fast waves incident on material boundaries

D. A. D'Ippolito and J. R. Myra

Lodestar Research Corporation, 2400 Central Avenue, Boulder, Colorado 80301

E. F. Jaeger and L. A. Berry

Oak Ridge National Lab, Oak Ridge, Tennessee

May, 2007; revised July, 2008

DOE/ER/54392-38 & ER/54823-2

LRC-07-113

Lodestar Research Corporation
2400 Central Avenue, Boulder, CO 80301

Far-field sheaths due to fast waves incident on material boundaries*

D. A. D’Ippolito† and J. R. Myra

Lodestar Research Corporation, 2400 Central Avenue, Boulder, Colorado 80301

E. F. Jaeger and L. A. Berry

Oak Ridge National Lab, Oak Ridge, Tennessee

Abstract

The problem of “far-field” sheath formation is studied with a new quantitative one-dimensional model. These radiofrequency (rf) sheaths occur when unabsorbed fast waves in the ion cyclotron range of frequencies are incident on a conducting surface not aligned with a flux surface. Use of a nonlinear sheath boundary condition gives self-consistent solutions for the wave fields and sheath characteristics, and it introduces a sheath-plasma-wave resonance which can enhance the sheath potential. The model is used to compute the parametric dependence of the far-field sheath potential. Its application to post-process the rf fields computed by a full-wave code for a typical D(H) minority heating scenario is also discussed. This work shows that 2D effects (included heuristically) are essential in determining whether far-field sheath potentials are strong enough to cause significant edge interactions, such as impurity generation and reduced heating efficiency.

PACS numbers: 52.35.Mw, 52.40.Kh, 52.50.Qt, 52.55.Fa

†email: dippolito@lodestar.com

I. Introduction

The ability of radiofrequency (rf) waves in the ion cyclotron range of frequency (ICRF) to heat fusion plasmas under a wide range of plasma conditions has been successfully demonstrated on many experiments. There is also a great deal of interest in using ICRF antennas to drive steady-state currents in tokamaks, which requires a low- k_{\parallel} spectrum to achieve the required resonance with energetic electrons. In practice, this is achieved by using a fast wave (FW) antenna with multiple (more than two) straps and a small relative phase difference $\Delta\phi$ between adjacent current straps. It has been observed on many ICRF experiments that “low- k_{\parallel} phasing” of the antenna (small $\Delta\phi$) leads to reduced coupling efficiency¹⁻⁷ of the waves to the core plasma and increased edge interactions (impurity generation and power dissipation in the edge plasma). In FW heating experiments, this effect is clearly seen in comparing monopole ($\Delta\phi = 0$) and dipole ($\Delta\phi = \pi$) phasing of two-strap antennas. The origin of the *phasing dependence* of the heating efficiency is one of the unsolved problems in ICRF research and partly motivates the work in this paper.

A large body of theoretical and experimental work over the past thirty years has shown that many of deleterious ICRF-edge plasma interactions are due to the coupling of the launched FW to the unwanted slow wave (SW) by various linear and nonlinear mechanisms (for reviews of this literature, see Refs. 8 and 9). One of the most important nonlinear effects is *rf sheath formation*, in which the SW accelerates electrons parallel to the magnetic field, thereby increasing the sheath potential needed to maintain ambipolarity. The sheath potential provides a spatially extended source of both impurities and power dissipation, because ions accelerated down the sheath potential can sputter wall material and deposit their energy in the material boundaries around the plasma.

The sheath formation process depends on the relative angle of the magnetic field with respect to surrounding material structures. To put the present work in context, it is useful to distinguish several types of sheaths. Sheaths on the antenna surface and on

nearby limiters are often referred to as “*near-field sheaths*”. These occur when the equilibrium magnetic field \mathbf{B} is not perpendicular to the active elements in the antenna (e.g. current straps and feeders) so that the rf electric field \mathbf{E}_{rf} has a component E_{\parallel} parallel to \mathbf{B} . It has been shown that near-field sheath formation is minimized by symmetry, e.g. with $\Delta\phi = \pi$ for the relative phasing of two adjacent straps (“dipole phasing”) and is maximized when $\Delta\phi \rightarrow 0$.¹⁰⁻¹³ Thus, near-field sheath effects are largest in low- k_{\parallel} phasing. “*Far-field sheaths*” occur when two conditions are satisfied: (i) a launched FW propagates into a wall, e.g. through or around the core plasma, but is not fully absorbed; and (ii) the magnetic field has a mismatch with material surfaces around the boundary of the machine (“the wall”). This mismatch occurs when \mathbf{B} has a component normal to the wall, which couples the FW to the SW through a boundary condition (BC) obtained from Maxwell’s equations. Again, the SW has a non-zero E_{\parallel} , which accelerates electrons into the boundary and increases the local sheath potential. Far-field sheath effects are also largest in low- k_{\parallel} phasing, because the single pass damping (and isolation of the far wall from the FW fields) typically increases with k_{\parallel} . Sheaths can also be driven by surface waves and coaxial modes,^{7,8} which also favor low k_{\parallel} , or they can arise on field lines that connect to spatial regions in which such waves are present.¹⁴

There has been a great deal of work on near-field (and, in particular, antenna) sheaths (see Ref. 9 and references therein). Far-field sheaths have received much less attention, and we do not yet know the answer to the following questions: Do far-field sheaths contribute significantly to the “missing power” (reduced core heating efficiency) in ICRF experiments? Are they partly responsible for the observed phasing dependence of the heating efficiency? Do they contribute to the impurity content of the SOL and core plasmas? Quantitative numerical models are needed to answer these questions.

The basic mechanism of far-field sheath formation was described by Perkins¹⁵ and studied numerically in Ref. 16. The BC on the rf field used in these papers is that the component \mathbf{E}_t of the rf electric field tangential to the wall must vanish on the boundary.

This BC is valid when the wall is assumed to be perfectly conducting and the sheath capacitance effect is negligible. As noted above, it was shown that the Maxwell BCs cannot be satisfied by the FW alone unless the wall shape conforms to a magnetic flux surface, which is typically not a good assumption.

The present paper develops a quantitative one-dimensional (1D) model of far-field sheath formation which extends the previous work^{15,16} in several respects. First, the sheath capacitance is taken into account by treating the sheath as a thin vacuum region separating the plasma and the wall. The sheath capacitance adds another term to the BC which the rf fields must satisfy.^{16,17} This “sheath BC” (in the form derived in Ref. 17) is then incorporated into an analytic wave-scattering calculation at the wall. We assume that the incident FW generates a reflected FW and a (typically evanescent) SW at the wall, and the three-wave coupling problem is solved at the sheath-plasma interface. As the sheath BC is nonlinear, a numerical root finding procedure is used to determine self-consistently the rf sheath width, sheath potential, and the normal component of the rf electric field on the plasma-side of the sheath-plasma boundary. The model developed here can be used for parameter studies and to post-process the results of linear rf codes to estimate the nonlinear effects at the far wall.

The sheath BC modifies the rf wave physics in two ways: (i) it modifies the distribution of E_{\parallel} between the plasma and the sheaths,¹⁷ and (ii) the sheath capacitance allows a new class of modes in the sheath-plasma system, “sheath-plasma-waves” (SPW).¹⁸⁻²⁰ We will show that the SPW can provide a resonant enhancement of the far-field sheaths (see Sec. IV).

The plan of this paper is as follows. The wave scattering model is described in Sec. II and the physics of the SPW resonance is discussed in Sec. III. It is shown that the resonance occurs for short wavelength poloidal or toroidal modes. Two mechanisms for generating these modes are discussed in Sec. III and Appendix A. The model is applied to a typical D(H) minority heating case for a DIII-D-size tokamak in Sec. IV with input

fields to the sheath model determined by matching the output of the AORSA-1D full-wave code.²¹ Finally, a summary and our conclusions are given in Sec. V. In Appendix A, a discussion is given of the effect of linear mode coupling at the boundary in generating higher mode numbers of the reflected FW (making sheath-plasma-wave resonance more likely).

II. Wave scattering model

A. Formulation of the problem

We consider the problem of a propagating fast wave in 1D geometry encountering a sheath, modeled here as an equivalent lossy vacuum region. We assume that an incident FW travels in the negative x -direction and couples to additional rf waves upon encountering the sheath-plasma boundary at $x = 0$. The boundary is *not* assumed to coincide with a magnetic flux surface, i.e.

$$\mathbf{s} \cdot \mathbf{b} \neq 0 \quad , \quad (1)$$

where $\mathbf{s} = \hat{\mathbf{e}}_x$ is the unit vector normal to the sheath (pointing into the plasma), and $\mathbf{b} = \mathbf{B}/B$ is the unit vector along the B-field direction. (See Fig. 1.)

If we neglect the presence of the sheath, Maxwell's equations impose the well-known *conducting wall BC* on the rf electric field at the wall

$$\mathbf{E}_t \equiv (\mathbf{s} \times \mathbf{E}) \times \mathbf{s} = (\mathbf{I} - \mathbf{ss}) \cdot \mathbf{E} = 0 \quad \Rightarrow \quad \mathbf{s} \times \mathbf{E} = 0 \quad . \quad (2)$$

This BC can be generalized to include the effect of the sheath by modeling the sheath as a thin lossy vacuum region of width Δ separating the wall and the plasma. The *rf sheath BC*^{16,17} is given by

$$\mathbf{s} \times \mathbf{E} = \mathbf{s} \times \nabla \left(\frac{\Delta}{\epsilon_{\text{sh}}} \mathbf{s} \cdot \mathbf{D} \right) \equiv \mathbf{s} \times \nabla \left(\frac{\Delta}{\epsilon_{\text{sh}}} D_n \right) \quad , \quad (3)$$

where the subscripts “n” and “t” refer to the components normal and tangential to the surface, Δ is the time-averaged (dc) sheath width, and $\epsilon_{\text{sh}} = 1 + i\nu$ is the scalar dielectric for the “lossy vacuum” sheath model. The right-hand side (rhs) of the rf sheath BC includes the effect of the sheath capacitance ($\propto \Delta$) and the sheath resistance ($\propto \nu$), and it reduces to the conducting wall BC in the limit $\Delta \rightarrow 0$. This BC is derived from the requirements that D_n and E_t be continuous across the sheath-plasma interface treating the sheath as a thin vacuum layer.^{16,17}

If $\mathbf{s} \cdot \mathbf{b} \neq 0$, the incident FW (denoted by subscript 0) will not satisfy either the conducting wall or sheath BC without coupling to additional waves. Here, we consider a minimal three-wave coupling model in which there is also a reflected FW (subscript 1) and a (possibly evanescent) slow wave (SW, subscript 2) at the boundary. For simplicity, we assume that the density $n(x)$ is constant near the wall, and the homogeneous plasma dispersion relations are used. The total rf electric field is given by

$$\mathbf{E} = e^{i(k_y y + k_z z - \omega t)} \sum_{j=0}^2 E_j \mathbf{e}_j e^{ik_x x} . \quad (4)$$

where the vectors without carats, \mathbf{e}_j ($j=0,1,2$), are the wave polarization unit vectors, not to be confused with the Cartesian unit vectors, $\hat{\mathbf{e}}_j$ ($j=x,y,z$). We assume that $\mathbf{k}_t = (k_y, k_z)$ is specified and the k_x components are obtained from the appropriate dispersion relations, as discussed in the next section.

Substituting the \mathbf{E} field in Eq. (4) into the sheath BC in Eq. (3) with $\epsilon_{\text{sh}} = 1$ (neglecting sheath resistivity) and $x = 0$, we obtain the following relations among the field amplitudes

$$\sum_{j=0}^2 E_j \mathbf{s} \times \mathbf{g}_j = 0 , \quad (5)$$

$$\mathbf{g}_j = \mathbf{e}_j - i\Delta (\mathbf{s} \cdot \boldsymbol{\epsilon} \cdot \mathbf{e}_j) \mathbf{k}_j . \quad (6)$$

where ϵ is the plasma dielectric tensor. The two constraints in Eqs. (5) and (6) determine the unknowns E_1 and E_2 in terms of the incident FW amplitude E_0 . Dotting Eq. (5) with \mathbf{g}_1 and \mathbf{g}_2 yields the solutions for the secondary waves at the boundary

$$\text{FW: } E_1 = E_0 \frac{\mathbf{s} \cdot \mathbf{g}_2 \times \mathbf{g}_0}{\mathbf{s} \cdot \mathbf{g}_1 \times \mathbf{g}_2}, \quad \text{SW: } E_2 = E_0 \frac{\mathbf{s} \cdot \mathbf{g}_0 \times \mathbf{g}_1}{\mathbf{s} \cdot \mathbf{g}_1 \times \mathbf{g}_2}. \quad (7)$$

Equations (6) and (7) show that the coupling to the SW occurs even in the absence of the sheath capacitance term ($\Delta \rightarrow 0$). The role of the sheath term will be discussed in Sec. III.

For the sake of simplicity, in Eq. (4) we assume that all three waves have the same values of $\mathbf{k}_t = (k_y, k_z)$. This assumption is not true in the case where the boundary is “bumpy” with variation on scales much shorter than the wavelength of the incident wave. In this case, linear mode coupling produces reflected waves at various spatial harmonics (see Appendix A). This physics is incorporated heuristically in the present model by allowing \mathbf{k}_t to be large.

B. Wave propagation

The wave coupling solution depends on the linear wave theory through the eigenvectors $\hat{\mathbf{e}}_j$ in Eqs. (5) -(7). Our code solves the cold plasma wave equations²²

$$\mathbf{n} \times (\mathbf{n} \times \mathbf{E}) + \epsilon \cdot \mathbf{E} = 0 \quad (8)$$

where $\mathbf{n} = \mathbf{k}c/\omega$ is the index of refraction and ϵ is the cold plasma dielectric tensor. In the reference frame (ξ, η, \mathbf{b}) defined as

$$\xi = \frac{\mathbf{k}_\perp}{|\mathbf{k}_\perp|}, \quad \eta = \frac{\mathbf{b} \times \mathbf{k}_\perp}{|\mathbf{k}_\perp|}, \quad \mathbf{b} = \frac{\mathbf{B}}{|\mathbf{B}|}, \quad (9)$$

the dielectric tensor has the form derived by Stix²²

$$\epsilon = \begin{pmatrix} \epsilon_\perp & -i\epsilon_x & 0 \\ i\epsilon_x & \epsilon_\perp & 0 \\ 0 & 0 & \epsilon_\parallel \end{pmatrix}, \quad (10)$$

$$\epsilon_{\perp} = 1 - \frac{\omega_{pi}^2}{(\omega^2 - \Omega_i^2)} , \quad \epsilon_{\parallel} = 1 - \frac{\omega_{pe}^2}{\omega^2} , \quad \epsilon_x = \frac{\omega_{pi}^2 \omega}{\Omega_i (\omega^2 - \Omega_i^2)} . \quad (11)$$

In a homogeneous (constant-density) plasma, the wave equation yields a 4th order dispersion relation for the four coupled fast and slow waves

$$\text{Det} \left| \boldsymbol{\epsilon} + \mathbf{nn} - n^2 \mathbf{I} \right| = 0 . \quad (12)$$

The k_x roots for each wave are chosen according to the following rules. For the incident fast wave ($k_x = k_{x0}$), we pick the propagating or evanescent root that has

$$\begin{aligned} \text{Im}[k_x] &< 0 , \\ \text{If } \text{Im}[k_x] &= 0, \text{ then } \text{Re}[k_x] < 0 . \end{aligned} \quad (13)$$

For the reflected FW ($k_x = k_{x1}$) and the SW ($k_x = k_{x2}$), we pick the roots that have

$$\begin{aligned} \text{Im}[k_x] &> 0 , \\ \text{If } \text{Im}[k_x] &= 0, \text{ then } \text{Re}[k_x] > 0 . \end{aligned} \quad (14)$$

The corresponding wave polarization unit vectors are given by

$$\mathbf{e}_0 = \mathbf{e}_{FW}(n_{x0}) , \quad \mathbf{e}_1 = \mathbf{e}_{FW}(n_{x1}) , \quad \mathbf{e}_2 = \mathbf{e}_{SW}(n_{x2}) . \quad (15)$$

where $\mathbf{e}_{FW}(n_x)$ and $\mathbf{e}_{SW}(n_x)$ (not shown) denote the eigenvectors of the 4th order problem, which, in general, must be obtained numerically.

C. Limiting Cases

For physical insight, it is often useful to consider the approximate 2nd order dispersion relations for the uncoupled fast and slow waves

$$\begin{aligned} \text{FW: } n_{\perp}^2 (n_{\parallel}^2 - \epsilon_{\perp}) + (n_{\parallel}^2 - \epsilon_{\perp})^2 - \epsilon_x^2 &= 0 , \\ \text{SW: } n_{\parallel}^2 \epsilon_{\parallel} + \epsilon_{\perp} (n_{\perp}^2 - \epsilon_{\parallel}) &= 0 , \end{aligned} \quad (16)$$

where the indices of refraction n_{\perp} and n_{\parallel} both contain the unknown $n_x = k_x c / \omega$. The fast wave obeys the ordering $n_{\perp}^2 \sim \epsilon_{\perp}, \epsilon_x \ll \epsilon_{\parallel}$ and the SW ordering is $n_{\perp}^2 \sim \epsilon_{\parallel} \gg \epsilon_{\perp}, \epsilon_x$.

The corresponding polarization unit vectors are given by¹⁶

$$\mathbf{e}_{\text{FW}} = \frac{Q\mathbf{n}_{\perp} + \mathbf{b} \times \mathbf{n}_{\perp}}{|Q\mathbf{n}_{\perp} + \mathbf{b} \times \mathbf{n}_{\perp}|}, \quad Q = \frac{-i\epsilon_x}{(n_{\parallel}^2 - \epsilon_{\perp})}, \quad (17)$$

$$\mathbf{e}_{\text{SW}} = \frac{G\mathbf{n}_{\perp} + \mathbf{b}}{|G\mathbf{n}_{\perp} + \mathbf{b}|}, \quad G = \frac{n_{\parallel}}{(n_{\parallel}^2 - \epsilon_{\perp})}. \quad (18)$$

It is useful to examine the scaling of the reflected slow wave in the limits $\Delta \rightarrow 0$ (metal wall BC) and $n_{\parallel}^2 \gg \epsilon_{\perp}$ (vacuum FW, electrostatic SW). In this limit, we find

$$\mathbf{e}_0 \rightarrow \frac{\mathbf{b} \times \mathbf{n}_0}{|\mathbf{b} \times \mathbf{n}_0|}, \quad \mathbf{e}_1 \rightarrow \frac{\mathbf{b} \times \mathbf{n}_1}{|\mathbf{b} \times \mathbf{n}_1|}, \quad \mathbf{e}_2 \rightarrow \frac{\mathbf{n}_2}{|\mathbf{n}_2|}. \quad (19)$$

The denominator in the expression (7) for E_2 reduces to

$$\mathbf{s} \cdot \mathbf{g}_1 \times \mathbf{g}_2 \rightarrow \mathbf{s} \cdot \mathbf{e}_1 \times \mathbf{e}_2 \approx \frac{(\mathbf{s} \cdot \mathbf{n}_1)(\mathbf{b} \cdot \mathbf{n}_2) - (\mathbf{s} \cdot \mathbf{b})(\mathbf{n}_1 \cdot \mathbf{n}_2)}{(|\mathbf{b} \times \mathbf{n}_1|) |\mathbf{n}_2|}. \quad (20)$$

which does not vanish for the assumed polarizations. The numerator of E_2 becomes

$$\mathbf{s} \cdot \mathbf{g}_0 \times \mathbf{g}_1 \rightarrow \mathbf{s} \cdot \mathbf{e}_0 \times \mathbf{e}_1 \propto (\mathbf{s} \cdot \mathbf{b})(\mathbf{b} \cdot \mathbf{n}_0 \times \mathbf{n}_1). \quad (21)$$

Writing $\mathbf{n}_1 = \mathbf{n}_0 + (n_{1x} - n_{0x})\hat{\mathbf{e}}_x$, we can show that $\mathbf{b} \cdot \mathbf{n}_0 \times \mathbf{n}_1 \approx (n_{0x} - n_{1x})n_{0y}b_z$ and

$$E_2 \propto (n_{0x} - n_{1x})n_{0y}b_x b_z. \quad (22)$$

The form given in Eq. (22) shows that there are several requirements for coupling to the SW in the present model for the sub-limits under discussion (low density, negligible sheaths). First, there must be a mismatch between the flux surface and the wall shape ($\mathbf{s} \cdot \mathbf{b} = b_x \neq 0$). Second, there must be incident and reflected FWs propagating in opposite directions, so that $(n_{1x} - n_{0x}) \neq 0$. Finally, the incident FW should have a component in the $\mathbf{s} \times \mathbf{b}$ direction: in the geometry assumed here, this implies $n_{0y} \neq 0$. The fact that the slow wave amplitude is proportional to k_y is important, and partly motivates the discussion of linear mode coupling due to wall geometry in Appendix A.

D. Sheath Potential and Power Dissipation

Given a solution for the scattered rf wave fields, it is straightforward to obtain the sheath width, the self-consistent potential drop across the sheath, and the power dissipated by the sheaths. Here, we consider only the “sheath power dissipation” due to ions which are accelerated in the sheath and deposit their energy in the wall (see e.g. Ref. 23).

Given a specified value of the sheath width Δ , an expression for the rf sheath potential Φ_{rf} can be obtained by matching the normal component of \mathbf{D} across the sheath-plasma interface. Treating the sheath as a thin vacuum region ($\epsilon_{\text{sh}} = 1 \Rightarrow D_{\text{n}}^{(\text{sh})} = -\Phi_{\text{rf}} / \Delta$) and using an expression for \mathbf{D}_{n} in the plasma obtained from Eq. (4), we find

$$\Phi_{\text{rf}} \equiv \Delta \left| \sum_{j=0}^2 E_j \mathbf{s} \cdot \boldsymbol{\epsilon}_j \cdot \mathbf{e}_j \right|. \quad (23)$$

Note that the value of Δ isn't known *a priori* and must be solved for self-consistently as part of the algorithm.

It is well-known that the total dc sheath potential $\Phi_{\text{sh}} \equiv C_{\text{sh}} \Phi_{\text{rf}} + \Phi_{\text{B}}$ (including both rf and Bohm sheath contributions) must satisfy the Child-Langmuir (CL) Law

$$\Phi_{\text{sh}}^{(\text{CL})} \equiv \frac{T_e}{e} \left(\frac{\Delta}{\lambda_{\text{D}}} \right)^{4/3}. \quad (24)$$

Here, $C_{\text{sh}} \Phi_{\text{rf}}$ is the rectified (time-averaged) rf sheath potential, C_{sh} is an order-unity rectification factor ($C_{\text{sh}} \approx 0.6$ for 0-to-peak voltages²⁴ in the limit $\Phi_{\text{rf}} \gg \Phi_{\text{B}}$), Φ_{B} is the Bohm (thermal) sheath potential defined subsequently, and $\lambda_{\text{D}} = (T / 4\pi n e^2)^{1/2}$ is the Debye length.

Equation (24) exhibits the scaling $\Phi_{\text{sh}} \propto \Delta^{4/3}$, and thus a nonlinear rootfinder must be used to obtain self-consistent values of the sheath width and potential that solve

Eqs. (23) and (24) simultaneously. The self-consistent solution requires that Φ_{rf} in Eq. (23) satisfy $C_{\text{sh}}\Phi_{\text{rf}} \rightarrow \Phi_{\text{sh}}^{(\text{CL})} - \Phi_{\text{B}}$, where the Bohm potential is given by²⁵

$$\Phi_{\text{B}} = \frac{T_e}{e} \ln[(m_i/m_e)^{1/2} \sin \alpha] . \quad (25)$$

This expression is valid when $(m_e/m_i)^{1/2} < \sin \alpha < 1$, where $\sin \alpha = \mathbf{s} \cdot \mathbf{b} \equiv B_x / B$.

The sheath power dissipation carried out of the plasma by ions accelerated in the dc sheath potential is given by

$$P_{\text{sh}} \equiv Zn_i c_s (3T_e) \xi h(\xi) \frac{I_1(\xi)}{I_0(\xi)} A_{\perp} \rightarrow C_{\text{sh}} n_i c_s Ze\Phi_{\text{rf}} A_{\perp}, \quad (26)$$

where $\xi \equiv Ze\Phi_{\text{rf}}/T_e$, $A_{\perp} = |\mathbf{s} \cdot \mathbf{b}| A$ is the area of the sheaths normal to \mathbf{B} , and A is the surface area of the sheaths. The first expression for P_{sh} was derived in Ref. 23 for modeling the transition from the Bohm ($\xi \sim 1$) to the strong rf-sheath ($\xi \gg 1$) regime; the second expression in Eq. (26) gives the $\xi \gg 1$ limit.²⁴ Here, $h(\xi) = (0.5 + C_{\text{sh}} \xi)/(1 + \xi)$ is a form factor connecting known results in the $\xi \ll 1$ and $\xi \gg 1$ limits. In the calculations presented here, our goal is to identify parameter regimes in which the far-field sheath potential is dominated by the rf contribution, so for simplicity we take the $\xi \gg 1$ limit in Eq. (26).

Finally, we can calculate the resistive part of the sheath dielectric as follows:

$$\epsilon_{\text{sh}} = 1 + i\nu \quad , \quad \nu = \frac{8\pi\Delta(P_{\text{sh}}/A_{\perp})}{\omega\Phi_{\text{sh}}^2} . \quad (27)$$

In this paper we assume $\nu \ll 1$ and set $\epsilon_{\text{sh}} = 1$ [starting in Eq. (6)]. Combining Eqs. (26) and (27), one can show that $\nu \propto 1/\Phi_{\text{sh}}$ and thus the small- ν approximation tends to be valid in the strong sheath limit.

III. Sheath plasma wave resonance

When the sheath width Δ is large enough that the two terms in \mathbf{g}_j are comparable [see Eq. (6)], the denominator $\mathbf{s} \cdot \mathbf{g}_1 \times \mathbf{g}_2$ can become small in Eq. (7). This produces a resonant enhancement of the sheath potential for some locus of points in the $\mathbf{n}_\perp = (n_y, n_z)$ parameter space. In Sec. IV.A we show that the resonance is related to a class of modes called “sheath plasma waves,”¹⁸⁻²⁰ which appear when the sheath capacitance is retained. These surface waves were studied and simulated in Ref. 20 in connection with near-field sheaths on ion-Bernstein wave antennas. Here, they appear in the context of far-field sheaths generated by propagating fast waves.

The SPW resonance requires

$$(\mathbf{s} \cdot \boldsymbol{\varepsilon} \cdot \mathbf{e}_j) \mathbf{k}_j \Delta \sim 1, \quad (28)$$

which for typical FW parameters means $|\mathbf{n}_\perp| \gg 1$. The resonance condition can only be satisfied when the sheath width Δ is finite, so it involves the sheath capacitance in an essential way. Physically, the SPW resonance occurs because the inductive plasma current into the sheath due to ε_{\parallel} (with inductance L) and the capacitive current across the sheath (with capacitance C) form a resonant LC circuit for some parameters.¹⁸

We first examine the resonance with the sheath width Δ fixed, and then carry out the nonlinear solution for the self-consistent values of Δ .

A. Fixed Δ

Equation (5) determines the field amplitudes E_1 and E_2 driven by a given incident FW E_0 . Near the resonance $\mathbf{s} \cdot \mathbf{g}_1 \times \mathbf{g}_2 = 0$ one can find two normal modes of the coupled sheath-plasma system which have large amplitudes.

The existence of nearly-resonant contributions is shown in Fig. 2, where two contours of the normalized SW amplitude, $|E_2/E_0|$, are plotted in the (n_y, n_z) plane. In carrying out the wave-scattering calculation, the density n_e , electron temperature T_e , magnetic field B , magnetic mismatch parameter B_x/B , and incident FW field E_0 are

specified at the sheath-plasma interface. The parameters used in Fig. 2 are $n_e = 1 \times 10^{12} \text{ cm}^{-3}$, $T_e = 10 \text{ eV}$, $B = 30 \text{ kG}$, $B_x/B = 0.2$, $f = 60 \text{ MHz}$ (rf frequency), and $E_0 = 10 \text{ V/cm}$. This case is similar to the one studied in Sec. IV.

In Fig. 2, the contours $|E_2/E_0| = 5$ (solid line) and 6 (dashed line) are plotted for two values of the sheath width Δ to show the region of parameter space where the slow wave amplitude is enhanced by the SPW resonance. The location of the resonance depends on the sheath width Δ , which was specified here as an input parameter, but will be solved for self-consistently in the next section. Fig. 2 shows that smaller Δ requires larger values of n_y or n_z (or higher density) to obtain resonance. The density scaling is given by the dependence on the cold-plasma dielectric tensor ϵ_j given in Eq. (28). For fixed Δ , Eq. (28) also shows that the resonance condition is independent of T_e at the sheath-plasma interface.

An examination of the numerical solution shows that the SPW undergoes a transition in moving from the upper left hand corner to the lower right hand corner in Fig. 2. In the limit $n_y \gg n_z$, $|\mathbf{s} \cdot \mathbf{g}_1 \times \mathbf{g}_2|$ can be small because $\mathbf{g}_1 \times \mathbf{g}_2$ is orthogonal to \mathbf{s} , although neither \mathbf{g}_1 or \mathbf{g}_2 is individually small. In this limit the SPW involves a coupling of the FW and the SW and is therefore fundamentally *electromagnetic*. In the limit $n_x \gg n_z \gg n_y$, the SPW is an *electrostatic* (ES) slow wave satisfying $n_\perp \sim n_x \gg n_\parallel$, and the plasma approaches resonance because the tangential component of \mathbf{g}_2 is small.

1. *Electromagnetic SPW resonance*

The electromagnetic (EM) limit of the SPW resonance can occur in at least two situations, which we now discuss.

First, we consider low-single pass absorption cases, where the wave fronts make many passes across the plasma, reflecting off the FW cutoff layer in the low-density edge plasma. In the multiple-pass case, the poloidal mode number spectrum spreads during specular reflections at the boundary. Rf sheaths can form if the cutoff layer is sufficiently

close to the wall that a substantial fraction of the decaying rf field reaches the wall. Both numerical results from 2D wave propagation codes and simpler models²⁶ suggest that n_{\perp} isotropizes, giving $k_x \sim k_y \sim \pi/\delta_i$, where $\delta_i = c/\omega_{pi}$ is the ion skin depth (evaluated near the wall). Here, δ_i is the natural scale length for ICRF wave propagation (obtained by balancing $k^2 c^2/\omega^2 \sim \omega_{pi}^2/\omega^2$). We refer to this spectral broadening effect as “isotropization”.

An example of isotropization relevant to a DIII-D-like tokamak is shown in Fig. 3, where a low single-pass absorption case is compared with a high single-pass absorption case (both computed using the AORSA-2D full-wave code²⁷). For the low single pass case, the broadening of the poloidal mode spectrum is shown in Fig. 3(b) and the penetration of high-k rf waves to the plasma edge is shown in Fig. 3(d). The parameters used in this simulation ($n_{\text{edge}} = 8.5 \times 10^{12} \text{ cm}^{-3}$ and $f = 60 \text{ MHz}$) correspond to $k_y \sim \pi/\delta_i \sim 0.3 \text{ cm}^{-1} = 30 \text{ m}^{-1}$ and $n_y \sim 24$. The computed spectrum is a factor of 2 broader than this estimate.

The second situation in which an electromagnetic SPW resonance can occur is when a bumpy wall generates high k_y components (larger than those launched by the antenna) by the process of linear mode coupling, as illustrated in Appendix A (and also in Refs. 15 and 16). For this mechanism, the high k_y components of the FW are generated at the (bumpy) wall, and the evanescent layer for the rf fields to tunnel through can be smaller than in the isotropization case. The rf field at the wall is expected to be larger in this case.

Thus, either low single pass absorption or a mismatch of the wall shape with the flux surface can trigger the EM SPW resonance and enhance the formation of far-field sheaths.

2. Electrostatic SPW resonance

The identification of the resonance in Fig. 2 with the SPW considered in earlier papers is most easily done in the ES limit. To this end, consider the important case $n_{\perp}^2 \gg n_{\parallel}^2 \gg \epsilon_{\perp} \sim 1$, relevant to low-density edge plasmas. The first inequality yields the ES slow wave limit in which the tangential components of \mathbf{k}_2 and \mathbf{e}_2 are proportional, i.e. $(\mathbf{s} \times \mathbf{k}_2) \times \mathbf{s} = k_{2t} (\mathbf{s} \times \mathbf{e}_2) \times \mathbf{s}$. Taking this result and employing the definition of \mathbf{g}_2 , we write

$$\mathbf{s} \cdot \mathbf{g}_1 \times \mathbf{g}_2 = D_2(\omega, \mathbf{k}, \Delta) \mathbf{s} \cdot \mathbf{g}_1 \times \mathbf{e}_2 \quad , \quad (29)$$

so that the ES SW resonance condition is now

$$D_2(\omega, \mathbf{k}, \Delta) = 0 \quad (30)$$

with

$$D_2(\omega, \mathbf{k}, \Delta) \equiv 1 - i k_{2t} \Delta \mathbf{s} \cdot \boldsymbol{\epsilon} \cdot \mathbf{e}_2 \rightarrow 1 - i \Delta (k_{2t}/k_{2\perp}) \mathbf{s} \cdot \boldsymbol{\epsilon} \cdot \mathbf{k}_2 \quad . \quad (31)$$

The last form of D_2 is valid when the inequality $n_{\parallel}^2 \gg \epsilon_{\perp}$ applies, so that $G \rightarrow 1/n_{\parallel}$ and $\mathbf{e}_2 \rightarrow \mathbf{k}_2 / |\mathbf{k}_{2\perp}|$ by Eq. (19). In Appendix B, we show that Eqs. (30) and (31) reduce in certain limits to the electrostatic SPW dispersion relation derived in Ref. 20.

B. Self-Consistent Δ

Now we turn to the question of solving the nonlinear problem for the self-consistent rf sheath potential Φ_{rf} . We will show that the SPW resonance makes possible the existence of multiple roots for Φ_{rf} . The resonance is associated with the effect of the sheath capacitance term [Eq. (28)], and this term is enhanced by a large perpendicular component of the equilibrium B field normal to the wall, high density near the wall, high-k components in the wave spectrum, and strong rf wave fields. Here, we set $T_e = 10$ eV, $B = 30$ kG, $f = 60$ MHz, and study the dependence of the solution on the other parameters: indices of refraction (n_y, n_z), density at the wall n_e , normal magnetic field component (B_x/B) and incident FW amplitude at the wall (E_0).

It should be noted that the fast wave is typically radially evanescent in the edge region in the large n_y limit. In this case the FW dispersion relation [Eq. (16)] gives $n_{\perp}^2 \approx 0$ in lowest order, implying $n_x^2 \approx -n_y^2$, with the result that n_x is imaginary and depends only on n_y . It is remarkable that despite the evanescence of the rf field to modest values near the wall in our calculations, the SPW resonance still results in large values of the sheath potential. In the experiment, this situation could be realized through spectral broadening by a bumpy wall, where the region of high- k_y generation is likely to be confined to the region close to the wall (see Appendix A).

The simultaneous solution of Eqs. (23) and (24) for the rf sheath potential Φ_{rf} and sheath width Δ yields multiple roots in some parameter regimes. The self-consistent roots are defined by $D(\Delta) \equiv \Phi_{\text{rf}} - \Phi_{\text{sh}}^{(\text{CL})} = 0$, ensuring that the potential obeys the Child-Langmuir Law. To illustrate the root structure, in Fig. 4 we plot the difference function $D(\Delta)$ for the parameters $n_y = 30$, $n_z = 6$, $n_e = 2 \times 10^{12} \text{ cm}^{-3}$, $T_e = 10 \text{ eV}$, $B = 30 \text{ kG}$, $B_x/B = 0.2$, $f = 60 \text{ MHz}$ and $E_0 = 15 \text{ V/cm}$. There are three roots in this case.

The dependence of the three roots for the self-consistent Φ_{rf} on the index of refraction n_y is shown in Fig. 5 for the parameters $n_z = 6$, $n_e = 2 \times 10^{12} \text{ cm}^{-3}$, $T_e = 10 \text{ eV}$, $B = 30 \text{ kG}$, $B_x/B = 0.2$, and $E_0 = 20 \text{ V/cm}$. This figure shows the presence of three roots for $n_y < 30$. The resonance is very narrow for the highest two roots for small n_y . Because these roots are so closely spaced, dissipation or other physical effects not included in the present model would probably eliminate these roots, so they are not regarded as physically interesting. However, all three roots are well separated (and therefore probably physical) over the range $17 < n_y < 29$. For $n_y > 29$, the lowest two roots merge and the sheath potential jumps to the value of the highest root. Thus, Fig. 5 shows that the high- k parts of the wave spectrum make the largest contribution to the sheath potential. Finally, note that the self-consistent sheath potential of the upper root is much larger than typical Bohm sheath potentials.

In Fig. 6 we show the dependence of the self-consistent Φ_{rf} on B_x/B , where B_x is the component of the equilibrium magnetic field normal to the wall. This parameter characterizes the misalignment between the wall and the magnetic flux surfaces in our 1D model. The parameters used in Fig. 6 were $n_y = 30$, $n_z = 6$, $n_e = 2 \times 10^{12} \text{ cm}^{-3}$, $T_e = 10 \text{ eV}$, $B = 30 \text{ kG}$, and $E_0 = 20 \text{ V/cm}$. Again we see the presence of three roots (due to the SPW resonance) and an S-shaped curve leading to a much higher sheath potential for large values of the control parameter (here, B_x/B).

In Fig. 7, we plot the self-consistent Φ_{rf} vs the density in the boundary region near the wall for the parameters $n_y = 30$, $n_z = 6$, $T_e = 10 \text{ eV}$, $B = 30 \text{ kG}$, and $B_x/B = 0.2$. For the upper curve in Fig. 7, the denominator $|\mathbf{s} \cdot \mathbf{g}_1 \times \mathbf{g}_2|$ in Eq. (7) is reduced by more than a factor of 20 for the cases with the highest sheath potential. Figure 7 illustrates the dependence on both density and rf field strength.

Note also that a hysteresis effect occurs in Fig. 7. Because of the multiple root structure, starting at low density and raising n_e to $2 \times 10^{12} \text{ cm}^{-3}$ results in a lower sheath potential than starting at high density and lowering n_e to the same value. This may contribute in part to the common observation that machine conditioning is essential to good ICRF system performance.

We have also investigated the electrostatic SPW limit ($n_z^2 \gg n_y^2$) discussed in Sec. III A.2 for the base case parameters given above, but with $n_z = 30$ and $n_y = 6$. The plot (not shown here) is very similar to Fig. 7 except that the multiple root structure occurs at lower density (with Φ_{rf} peaking for $n_e = 0.5 \times 10^{12} \text{ cm}^{-3}$). Because z is nearly in the toroidal direction in tokamaks, this limit is relevant to tokamak experiments only when the walls or other hardware break the toroidal symmetry.

IV. Application to post-processing

In Sec. III, we showed that the wave-scattering (WS) model can be used to study the physics of far-field sheaths, including the self-consistency constraint on the sheath

potential imposed by the Child-Langmuir Law. The biggest uncertainty in this modeling is estimating the magnitude of the rf electric field at the boundary. One way around this problem is to use the WS scattering model to post-process the output of an rf full-wave code. In this section, we illustrate a way of obtaining quantitative estimates by using the AORSA-1D full-wave code²¹ to calculate the rf field profile. AORSA computes the wave propagation and absorption physics, determining how much of the FW field impinges on the far wall after passing through the core plasma.

The procedure is briefly summarized as follows. The AORSA-1D full-wave code²¹ (with metal wall BCs) is used to compute the rf field propagation across the plasma as a function of the distance from the wall, $x = R - R_w$. The amplitude of the binormal (approximately poloidal) FW electric field from AORSA-1D is fitted to a superposition of incident and reflected plane waves to obtain the part due to the incident wave near the wall, which is then used as input in our WS code to compute the sheath properties.

The AORSA wave propagation analysis is illustrated here for a *low-single-pass case* similar to the one shown in Fig. 3: D(H) minority ion heating with 2% H, $f = 60$ MHz, $B = 32.5$ kG (at HFS wall), toroidal mode number = 13, $k_y = 3 \text{ m}^{-1}$ ($\Rightarrow n_y = 2.4$ and $n_z = 6.3$), and $P_{\text{rf}} = 1$ MW. A model centrally-peaked density profile is assumed with a peak density of $n_{e0} = 6.3 \times 10^{13} \text{ cm}^{-3}$. The radial profile of the E_y (poloidal) component of the FW field is shown in Fig. 8. The AORSA-1D calculation employs the conducting-wall BC (obtained from the full sheath BC in the limit $\Delta \rightarrow 0$) at both ends, $R = 0.95$ m and $R = 2.2$ m. The antenna is located at $R = 2.18$ m, so that the wave propagates from right to left in this plot. The left-hand wall position is mapped to $x = 0$ in the local coordinate system of the WS model. Figure 8 shows that the wave reaches the far wall and sets up a standing wave because of the poor central absorption.

The procedure of fitting the FW amplitude near the wall yields $|E_0| = 44.5$ V/cm for the case shown in Fig. 8, corresponding to an input power of 1 MW. Note that this rf

E-field strength is about a factor of 2 larger than the value assumed in Figs. 4 – 7 in Sec. III. Thus, the AORSA calculation suggests that strong rf fields can reach the wall and far-field sheaths may be an issue.

We note that post-processing the full-wave code results with the wave scattering model would be unnecessary if we could implement the sheath BC directly into the wave propagation code itself.¹⁷ The motivation for the post-processing algorithm discussed in this section is that our attempt to implement the sheath BC (with $\Delta \neq 0$) in AORSA-1D has shown it to be a difficult numerical problem. There are three complications: (1) modifying the rf wave propagation code to allow a physical boundary (wall) that is not a flux surface; (2) numerically resolving the SW E_{\parallel} near the boundary (which varies rapidly in the radial direction, $L_x \sim \delta_e = c/\omega_{pe}$), and (3) iterating the rf field solution with the Child-Langmuir Law (or equivalently, using nonlinear rootfinding) to obtain the self-consistent sheath potential and associated rf fields near the boundary. These problems arise with all of the present full-wave codes, which were not built with edge physics issues in mind. New algorithms allowing the incorporation of the sheath BC directly into full wave codes is a subject for future work.

V. Summary and Discussion

Assessing and controlling the deleterious effects of rf sheath formation is important for optimizing ICRF heating and current drive in tokamaks. In some cases, sheath effects can reduce the heating efficiency, cause local heating of surfaces (“hot spots”), and generate high-Z impurities which cool the plasma core. All of these issues are especially important for the next generation of experiments and for ITER²⁸ because of the required high performance, the high power density and the need for long pulse operation. Thus, quantitative means of calculating sheath potentials in realistic magnetic geometries are needed.

The present paper provides a comprehensive treatment of the neglected problem of “far field sheaths,”¹⁶ which form on material boundaries not coincident with flux surfaces and located far from the antenna. The sheaths arise when rf fields are incident on the boundaries, either due to low single pass absorption in the core plasma or due to propagation nearly parallel to the magnetic field lines (e.g. around the SOL and into the divertor). Regarding the latter effect, it has been shown that the FW propagates nearly parallel to \mathbf{B} for high harmonic FW heating on NSTX.^{29,30} Simulations show that the propagating waves move a significant distance around the torus in the SOL before entering the core plasma, and the experiments show that wave coupling to the core plasma is improved by moving the density at which the FW begins to propagate ($n_e \propto Bk_{\parallel}^2 / \omega$) to a point further from the wall.^{29,30} These results suggest the presence of a parasitic power loss mechanism near the wall in NSTX, consistent with the picture of far field sheaths described here.

The two main contributions of this paper are:

- (1) the development of a new *quantitative* model for the far-field sheath potential; and
- (2) the discovery that *sheath-plasma-wave* resonances (well known in other contexts) play a role in enhancing the far-field sheath potential.

The wave-scattering model for far field sheaths (Sec. II) makes use of a sheath BC proposed earlier¹⁷ and gives a complete solution for the self-consistent slow wave that is generated at the wall and for the resulting sheath potential. The latter is constrained to satisfy the Child-Langmuir Law, given a specified incident FW field and assuming a homogeneous plasma near the wall. In Sec. III it was shown that the sheath capacitance introduces nonlinearity and additional roots into the sheath problem, which lead to sheath-plasma-wave resonances¹⁸⁻²⁰ for high-k wave components (Sec. III, Figs. 4-7). Possible mechanisms for generating high-k components include isotropization (Sec. III, Fig. 3) and linear mode coupling by a bumpy wall (Appendix A and Ref. 15), both of which are 2D or 3D effects. The new roots introduced by this resonance can have large

sheath potentials, above the level predicted by simple estimates. The effect of dissipation on resolving the SPW resonance, and thus limiting the sheath potential of the additional roots, is an interesting issue left for future work. In Sec. IV, we used the AORSA-1D code to demonstrate the procedure for calculating the inputs to the WS model, allowing post-processing of realistic rf cases. It was shown that the rf field at the far wall can be substantial for a typical DIII-D low-single-pass absorption case (Fig. 8).

Finally, we discuss the effect of far-field sheaths on important edge interactions such as power dissipation, local heating and sputtering of impurities. In Eq. (26), it was shown that the sheath power dissipation P_{sh} is linearly proportional to three factors: the local density at the wall, the surface area impacted by the rf waves, and the rectified sheath potential, $e\Phi_{\text{sh}} \sim 0.6 e\Phi_{\text{rf}} + 3T_e$. Using our wave-scattering model, the complicated parametric dependence of the sheath potential, $\Phi_{\text{sh}} = \Phi_{\text{sh}}(n_y, n_z, n_{\text{ew}}, B_x / B)$, was illustrated in Figs. 5–7. These 1D calculations indicate that far-field sheath potentials in the range of a few hundred volts are possible if the rf fields near the wall contain high-k components and the SPW resonance comes into play. However, this model cannot give us the spatial distribution of the waves around the tokamak, which requires at least a 2D calculation (see Fig. 3) and ultimately a 3D calculation for accurate results.

The present work suggests that far-field-sheath power losses may be important in present tokamaks in low single pass damping situations, but the answer depends on quantities that are not well known, e.g. the density near the wall. For power dissipation estimates in the limit $e\Phi_{\text{rf}} / T_e \gg 1$, Eq. (26) becomes²³

$$\frac{P_{\text{sh}}(\text{kW})}{A_{\perp}(\text{cm}^2)} = 1.0 \times 10^{-16} n_i(\text{cm}^{-3}) [ZT_e(\text{eV}) / \mu]^{1/2} Z e\Phi_{\text{rf}}(\text{eV}) \quad , \quad (32)$$

where all quantities are evaluated at the wall. Changing to MKS units and normalizing to a DIII-D-like case, we have

$$\frac{P_{\text{sh}}}{0.1 \text{ MW}} = \left(\frac{n_i}{10^{17} \text{ m}^{-3}} \right) \left(\frac{Z T_e / \mu}{5 \text{ eV}} \right)^{1/2} \left(\frac{Z e \Phi_{\text{rf}}}{100 \text{ eV}} \right) \left(\frac{A_{\perp}}{7 \text{ m}^2} \right), \quad (33)$$

For example, consider DIII-D-like plasma parameters similar to those used in Sec. III, an rf sheath potential of 100 V (consistent with some SPW resonance enhancement), and roughly 50% wall coverage by the rf waves with an average angle factor of $|\mathbf{s} \cdot \mathbf{b}| = 0.1$ (giving $A_{\perp} = 7 \text{ m}^2$ for a DIII-D size machine). Assuming an ion density near the wall in the range $n_i = 10^{17} - 10^{18} \text{ m}^{-3}$ yields a sheath power loss in the range 0.1 – 1.0 MW, a 10-100% effect on low power (1 MW) low-single pass current drive experiments. For ITER, the surface area is 10 times larger, but the density at the wall is unknown, so it is difficult to make a prediction. These examples illustrate the need for better (predictive) models of the SOL density profile including the effects of turbulence (blob transport), wall interactions, gas puffing for improved antenna coupling, etc.

Note that the power density (P_{sh}/A_{\perp}) is very small ($\sim 0.02 - 0.2 \text{ MW/m}^2$) over the same range in density; unlike antenna sheaths, this mechanism is not likely to cause hot spots unless the local density rises to $\sim 10^{19} \text{ m}^{-3}$, which might be possible with rf-induced outgassing.

Also interesting is the effect of far-field sheaths in enhancing first wall sputtering and increasing the plasma impurity content. Previous modeling¹⁰ of rf impurity production due to near-field sheaths showed the importance of the carbon background SOL impurity content for tokamaks with graphite limiters, and the importance of high-Z self-sputtering on surfaces with large sheath potentials. So we first consider low-Z impurity production, represented here by graphite (C) self-sputtering. We assume an ionization state of $Z = 3$ and $T_e = 10 \text{ eV}$ at the wall, so that the Bohm (thermal) sheath potential is $e\Phi_B = 3T_e = 30 \text{ eV}$. For a far-field sheath potential of $e\Phi_{\text{rf}} = 100 \text{ eV}$, the rf sheath effect is significant. In this region of sputtering energy E , the sputtering yield³¹ $Y(\text{C-C}) \sim 0.4$ is a factor 8.6 higher with the rf sheath contribution [$E = Ze(\Phi_B + \Phi_{\text{rf}})$]

than without it ($E = Ze\Phi_B$). For high- Z sputtering, represented here by Mo self-sputtering, the effect is even stronger. For $Z = 3$, the Mo^{+3} self-sputtering yield $Y(\text{Mo-Mo}) \sim 0.7$ including rf [$E = Ze(\Phi_B + \Phi_{\text{rf}})$] is a factor 56 higher than the Bohm sheath case, and it approaches the self-sputtering avalanche condition ($Y > 1$). For $Z = 5$, the Mo^{+5} self-sputtering yield crosses the avalanche threshold because of the rf far-field sheath contribution to the sputtering energy. Thus, we conclude that far field sheaths can increase the impurity content of the plasma, as inferred in an earlier analysis of titanium impurity data on TFTR.³²

For quantitative modeling, the present 1D treatment needs to be generalized to 2D to get the spatial distribution and spectral content of the rf fields at the wall and the spatial distribution of the sheath potential. One possible approach is to implement the rf sheath BC¹⁷ directly in a 2D full-wave code.

Acknowledgements

This work was carried out as part of the Scientific Discovery through Advanced Computing (SciDAC) project in radiofrequency wave-plasma interactions. We would like to thank the rf SciDAC team for their encouragement and advice on this project. One of the authors (DD) thanks T. Hellsten for a discussion of spectral broadening in low single pass wave propagation. This work was supported by the U.S. Department of Energy (DOE) under DOE Grants No. DE-FG02-97ER54392, DE-FC02-05ER54823 and No. DE-AC-5-00OR22725; however, this support does not constitute an endorsement by the DOE of the views expressed herein.

Appendix A Linear mode coupling

In the main text, we allowed the tangential component of the wavenumber, \mathbf{k}_t , near the wall to be much larger than \mathbf{k}_t of the FW launched from the antenna, arguing that the local effective wavenumber in our 1D model is determined partly by the shape of the

boundary through the process of linear mode coupling. In this Appendix, we illustrate the physics of linear mode coupling induced by a bumpy wall for a simple scalar wave problem.

Consider a model problem where an rf wave incident from the right reflects off of a bumpy wall. We wish to study the coupling to sideband modes, induced by the wall periodicity. Let the total wave solution be represented by the scalar Φ_{tot}

$$\Phi_{\text{tot}} = \Phi e^{iK_x x + iK_y y} + \sum_n \phi_n e^{ik_{nx} x + ik_{ny} y} \quad (\text{A1})$$

where upper-case letters (Φ, K_x, K_y) represent the incoming wave, lower-case letters (ϕ, k_x, k_y) represent the (outgoing / evanescent) wave, and \mathbf{k}_n is defined below. The equation of the bumpy wall is taken to be

$$x = x_w \sin k_w y \quad , \quad (\text{A2})$$

and we set $\Phi_{\text{tot}} = 0$ on the wall to satisfy the perfectly conducting wall BC imposed by Maxwell's equations. This constraint implies

$$\sum_n \phi_n e^{ik_{nx} x_w \sin k_w y + ik_{ny} y} = -\Phi e^{iK_x x_w \sin k_w y + iK_y y} \quad , \quad (\text{A3})$$

from which it can be seen [see also Eq. (A6) below] that the needed \mathbf{k}_n 's are

$$k_{ny} = K_y + nk_w \quad . \quad (\text{A4})$$

A dispersion relation, to be specified subsequently, gives $k_{nx} = k_{nx}(k_{ny})$ and also $K_x = K_x(K_y)$. We define

$$u_n = k_{nx} x_w \quad , \quad U = K_x x_w = -u_0 \quad , \quad (\text{A5})$$

and adopt the convention that the u_n are chosen as the outgoing / evanescent branch ($\text{Re } k_x > 0$ or $\text{Im } k_x > 0$) for the reflected waves. Hence, the incoming wave must have $\text{Re } K_x < 0$ and $U = -u_0$. Next we employ the identity

$$e^{iu_n \sin k_w y} = \sum_{m=-\infty}^{\infty} J_m(u_n) e^{imk_w y} \quad (\text{A6})$$

to rewrite Eq. (A3) as the matrix equation

$$\sum_{n=-\infty}^{\infty} J_{p-n}(u_n) \phi_n = -\Phi J_p(U) \quad (\text{A7})$$

Before considering the complete solution, it is useful to note the analytical result obtained when all the u_n are small. In that case, there is coupling to nearest neighbor sidebands because of the bump periodicity, but the coupling is weak:

$$\phi_0 / \Phi = -1 \quad , \quad \phi_{\pm 1} / \Phi = \pm u_0 \quad (\text{A8})$$

If $k_w \gg K_y$, the $n = 1$ sidebands might be sufficient to obtain an SPW resonant enhancement in the problem considered in the main text, but one would want $u_0 \approx 1$ to get a strong effect. This limit requires a full numerical solution of the matrix problem, which we now discuss.

Once a dispersion relation is specified to yield the u_n , Eq. (A7) provides the formal solution of the mode-coupling problem. However, in practice there is a complication. If the dispersion relation yields large complex k_{nx} for large n , then this solution is ill-posed because the Bessel functions become exponentially large. This issue is already apparent from Eq. (A3) for large complex k_{nx} and has its physical origin in the fact that waves exponentiate many times in x over a distance x_w . The matrix problem is *ill-posed* when the matrix contains elements of a disparate size, such that their manipulation leads to finite-precision truncation errors (e.g. in subtractive cancellation). Solving by spatial collocation, or using singular value decomposition, will not remedy this issue.

Instead, we choose a model dispersion relation which limits the shortest scale length that can be present for large n evanescent modes.

$$k_{nx}^2 = \frac{k_0^2 - (K_y + nk_w)^2}{1 + (\alpha nk_w x_w)^2} \quad (\text{A9})$$

where α is a dimensionless, nominally order unity, parameter that limits the size of $k_{nx}x_w$ to $\pm i \alpha$ at large n . In practice, we find that $\alpha = 0.2$ is a good compromise. Equation (A9) is also to be applied for the incoming wave, with $n = 0$ (choosing the appropriate sign of the square root). A sample numerical solution in the strong coupling limit is shown in Fig. A1. This solution shows that one can achieve strong coupling to sidebands ($\phi_{\pm 1} \approx \Phi$) even when $K_x x_w < 1$. In such cases, the values of the local indices of refraction (n_y, n_z) can be much larger than those of the launched fast wave.

Finally, we remark that a self-consistent 2D calculation of the far field sheath problem would contain all of the wave coupling physics studied in the present paper, unifying the three-wave treatment in the main body of the text with the mode coupling physics of this Appendix.

Appendix B Sheath Plasma Waves

In the main text, taking the limit $n_x \gg n_z \gg n_y$ we showed that the denominator in Eq. (7) for the rf electric field has the form

$$\mathbf{s} \cdot \mathbf{g}_1 \times \mathbf{g}_2 = D_2(\omega, \mathbf{k}, \Delta) \mathbf{s} \cdot \mathbf{g}_1 \times \mathbf{e}_2 \quad , \quad (\text{B1})$$

where D_2 is given by Eq. (31). Here, we show that $D_2(\omega, \mathbf{k}, \Delta)$ reduces in certain limits to the electrostatic sheath plasma wave (SPW) dispersion relation derived in Ref. 20.

For this comparison, we specialize to the case where the *magnetic field is normal to the sheath*, so that $\mathbf{b} = \mathbf{s}$ and $k_{2t} = k_{2\perp}$. (This would apply to far-field sheaths on poloidal limiters, and is also relevant to near-field antenna sheaths.) The square of Eq. (31) yields the condition $1 = -\Delta^2 (\mathbf{s} \cdot \boldsymbol{\epsilon} \cdot \mathbf{k}_2)^2 \approx -k_{\parallel}^2 \Delta^2 \epsilon_{\parallel}^2$. Recall that the ES SW wave vector components obey the infinite homogeneous dispersion relation

$$k_{\parallel}^2 \epsilon_{\parallel} + k_{\perp}^2 \epsilon_{\perp} = 0 \quad . \quad (\text{B2})$$

Combining the resonance condition and the constraint on the wavevector components, we obtain the dispersion relation for the resonant sheath-plasma modes, valid in the limit $n_{\perp}^2 \gg n_{\parallel}^2 \gg \epsilon_{\perp}$:

$$k_{\perp}^2 \Delta^2 \epsilon_{\parallel} \epsilon_{\perp} = 1 \quad . \quad (\text{B3})$$

After some manipulations, we can show that this resonance condition is identical to the electrostatic SPW dispersion relation derived in Ref. 20. In that paper, the magnetic field was assumed to connect two sheaths separated by a distance L , and \mathbf{B} was assumed to be normal to the sheaths. It is convenient to define the two parameters

$$\varpi \equiv -ik_{\parallel}L, \quad p \equiv \varpi \epsilon_{\parallel} / L \quad , \quad (\text{B4})$$

where we now have $k_{\parallel} = k_x$. The two sheaths uncouple as $\varpi \rightarrow \infty$, and the mode is evanescent in the x direction when ϖ is real. In the limit $\varpi \gg 1$, the SPW dispersion relation²⁰ reduces to $p\Delta \equiv \varpi(\Delta/L)\epsilon_{\parallel} = -1$. If we square this relation and use Eq. (B2), rewritten in the present notation as $\varpi = -ik_{\perp}L(-\epsilon_{\perp}/\epsilon_{\parallel})^{1/2}$, we find that the scale length L cancels out and we obtain Eq. (B3).

References

- ¹ D. F. H. Start, G. Bell, V. P. Bhatnagar, M. Bures, G. A. Cottrell, L.-G. Eriksson, B. Fechner, R. Goulding, C. Gormezano, A. Howman, J. Jacquinet, A. Kaye, P. Lamalle, F. Nguyen, E. Righi, F. Rimini, A. Sibley, A. C. C. Sips, B. J. Tubbing, T. Wade and D. Ward, *Proceedings of the 11th Topical Conference on Radio Frequency Power in Plasmas*, (AIP, New York, 1995), p. 7.
- ² J. Stevens, C. Busch, P. Colestock, G. Greene, K. Hill, J. Hosea, C. K. Phillips, B. Stratton, S. von Goeler, J. R. Wilson, W. Gardner, D. Hoffman and A. Lysojvan, *Plasma Phys. Controlled Fusion* **32**, 189 (1990).
- ³ J. C. Hosea, S. Bernabei, T. Biewer, B. LeBlanc, C. K. Phillips, J. R. Wilson, D. Stutman, P. Ryan, and D. W. Swain, *Proceedings of the 16th Topical Conference on Radio Frequency Power in Plasmas*, (AIP, New York, 2005), p. 82.
- ⁴ T. Hellsten, M. Laxåback, T. Bergkvist, T. Johnson, F. Meo, F. Nguyen, C.C. Petty, M. Mantsinen, G. Matthews, J.-M. Noterdaeme, T. Tala, D. Van Eester, P. Andrew, P. Beaumont, V. Bobkov, M. Brix, J.

- Brzozowski, L.-G. Eriksson, C. Giroud, E. Joffrin, V. Kiptily, J. Mailloux, M.-L. Mayoral, I. Monakhov, R. Sartori, A. Staebler, E. Rachlew, E. Tennfors, A. Tuccillo, A. Walden, K.-D. Zastrow and JET-EFDA Contributors, *Nucl. Fusion* **45**, 706 (2005).
- ⁵ P. U. Lamalle, M. J. Mantsinen, J.-M. Noterdaeme, B. Alper, P. Beaumont, L. Bertalot, T. Blackman, VI.V. Bobkov, G. Bonheure, J. Brzozowski, C. Castaldo, S. Conroy, M. de Baar, E. de la Luna, P. de Vries, F. Durodié, G. Ericsson, L.-G. Eriksson, C. Gowers, R. Felton, J. Heikkinen, T. Hellsten, V. Kiptily, K. Lawson, M. Laxåback, E. Lerche, P. Lomas, A. Lysoivan, M.-L. Mayoral, F. Meo, M. Mironov, I. Monakhov, I. Nunes, G. Piazza, S. Popovichev, A. Salmi, M.I.K. Santala, S. Sharapov, T. Tala, M. Tardocchi, D. Van Eester, B. Weysow and JET EFDA contributors, *Nucl. Fusion* **46**, 391 (2006).
- ⁶ L. Colas, V. Basiuk, B. Beaumont, A. Bécoulet, G. Bosia, S. Brémond, M. Chantant, F. Clairet, A. Ekedahl, E. Faudot, A. Géraud, M. Goniche, S. Heurax, G.T. Hoang, G. Lombard, L. Millon, R. Mitteau, P. Mollard, K. Vulliez and the Tore Supra team, *Nucl. Fusion* **46**, S500 (2006).
- ⁷ J. Hosea, R. E. Bell, B. P. LeBlanc, C. K. Phillips, G. Taylor, E. Valeo, J. R. Wilson, E. F. Jaeger, P. M. Ryan, J. Wilgen, H. Yuh, F. Levinton, S. Sabbagh, K. Tritz, J. Parker, P. T. Bonoli, R. Harvey, and NSTX Team, *Phys. Plasmas* **15**, 056104 (2008).
- ⁸ J.-M. Noterdaeme and G. Van Oost, *Plasma Phys. Control. Fusion* **35**, 1481 (1993).
- ⁹ J. R. Myra, D. A. D'Ippolito, D. A. Russell, L. A. Berry, E. F. Jaeger, and M. D. Carter, *Nucl. Fusion* **46**, S455-S468 (2006).
- ¹⁰ D. A. D'Ippolito, J. R. Myra, M. Bureš, and J. Jacquinot, *Plasma Phys. Controlled Fusion* **33**, 607 (1991).
- ¹¹ M. Bureš, J. Jacquinot, K. Lawson, M. Stamp, H. P. Summers, D. A. D'Ippolito and J. R. Myra, *Plasma Phys. Controlled Fusion* **33**, 937 (1991).
- ¹² M. Bureš, J. Jacquinot, M. F. Stamp, D. D. R. Summers, D. F. H. Start, T. Wade, D. A. D'Ippolito and J. R. Myra, *Nucl. Fusion* **32**, 1139 (1992).
- ¹³ J. R. Myra, D. A. D'Ippolito, and Y. L. Ho, *Fusion Eng. Design* **31**, 291 (1996).
- ¹⁴ M. Brambilla, R. Chodura, J. Hoffmann, and J. Neuhauser, in *Plasma Phys. Control. Nucl. Fusion Res.* 1990 (IAEA, Vienna, 1991), Vol. 1, p. 723.
- ¹⁵ F. W. Perkins, *Bull. Am. Phys. Soc.* **34**, 2093 (1989), paper 6S6.
- ¹⁶ J. R. Myra, D. A. D'Ippolito, and M. Bures, *Phys. Plasmas* **1**, 2890 (1994).
- ¹⁷ D. A. D'Ippolito and J. R. Myra, *Phys. Plasmas* **13**, 102508 (2006).
- ¹⁸ For an early discussion of the unmagnetized case, see G. Bekefi, *Radiation Processes in Plasmas* (Wiley, New York, 1966), pp. 168 – 173.
- ¹⁹ R. L. Stenzel, *Phys. Rev. Lett.* **60**, 704 (1988); *Phys. Fluids B* **1**, 2273 (1989) (and references therein).

- ²⁰ J. R. Myra, D. A. D'Ippolito, D. W. Forslund and J. U. Brackbill, *Phys. Rev. Lett.* **66**, 1173 (1991).
- ²¹ E. F. Jaeger, L. A. Berry, and D. B. Batchelor, *Phys. Plasmas* **7**, 3319 (2000).
- ²² T. H. Stix, *Waves in Plasmas*, AIP Press, (1992, Springer-Verlag, New York).
- ²³ D. A. D'Ippolito and J. R. Myra, *Phys. Plasmas* **3**, 420 (1996).
- ²⁴ J. R. Myra, D. A. D'Ippolito and M. J. Gerver, *Nucl. Fusion* **30**, 845 (1990).
- ²⁵ R. H. Cohen and D. D. Ryutov, *Plasma Phys. Repts.* **23**, 805 (1997).
- ²⁶ T. Hellsten, J. Källbäck and L.-G. Eriksson, in *Proceedings of the Twelfth Topical Conference on Radio Frequency Power in Plasmas*, (AIP, New York, 1997), p. 355.
- ²⁷ E. F. Jaeger, L. A. Berry, E. D'Azevedo, D. B. Batchelor, and M. D. Carter, *Phys. Plasmas* **8**, 1573 (2001).
- ²⁸ M. Shimada, D.J. Campbell, V. Mukhovatov, M. Fujiwara, N. Kirneva, K. Lackner, M. Nagami, V.D. Pustovitov, N. Uckan, J. Wesley, N. Asakura, A.E. Costley, A.J.H. Donné, E.J. Doyle, A. Fasoli, C. Gormezano, Y. Gribov, O. Gruber, T.C. Hender, W. Houlberg, S. Ide, Y. Kamada, A. Leonard, B. Lipschultz, A. Loarte, K. Miyamoto, V. Mukhovatov, T.H. Osborne, A. Polevoi and A.C.C. Sips, *Nucl. Fusion* **47**, S1 (2007).
- ²⁹ J. Hosea, R. E. Bell, B. P. LeBlanc, C. K. Phillips, G. Taylor, E. Valeo, J. R. Wilson, E. F. Jaeger, P. M. Ryan, J. Wilgen, H. Yuh, F. Levinton, S. Sabbagh, K. Tritz, J. Parker, P. T. Bonoli, R. Harvey, and NSTX Team, *Phys. Plasmas* **15**, 056104 (2008).
- ³⁰ P. M. Ryan, R. E. Bell, L. A. Berry, P. T. Bonoli, R. W. Harvey, J. C. Hosea, E. F. Jaeger, B. P. LeBlanc, C. K. Phillips, G. Taylor, E. J. Valeo, J. B. Wilgen, J. R. Wilson, J. C. Wright, H. Yuh, and the NSTX Team, *Proceedings of the 35th EPS Conference on Plasma Phys.*, Hersonissos, Greece, 9 - 13 June, 2008, ECA Vol.32, P-1.108 (2008)
- ³¹ see J. Bohdansky, in *Data Compendium for Plasma-Surface Interactions*, *Nucl. Fusion Special Issue* 1984; we use an analytic expression for the sputtering yield at normal incidence, Eq. (6.16) of this reference with empirical coefficients chosen to match the sputtering data [see Table 6.1].
- ³² D. A. D'Ippolito, J. R. Myra, J. H. Rogers, K. W. Hill, J. C. Hosea, R. Majeski, G. Schilling, J. R. Wilson, G. R. Hanson, A. C. England and J. B. Wilgen, *Nucl. Fusion* **38**, 1543 (1998).

Figure Captions

Fig. 1 Geometry of the scattering problem. An incoming fast wave (FW) generates a reflected FW and slow wave (SW) in order to satisfy the BC at the wall. The wave-coupling occurs when the B field has a projection normal to the wall ($\mathbf{s} \cdot \mathbf{b} \neq 0 \Rightarrow \alpha \neq 0$)

Fig. 2 Contour plot of the normalized SW amplitude, $|E_2/E_0|$, to illustrate the Sheath Plasma Wave (SPW) enhancement of the coupled waves. Shown are the contours $|E_2/E_0| = 5$ (solid line) and 6 (dashed line) for two values of the sheath width, $\Delta = 0.01$ and 0.03 cm, (not self consistent). The other parameters are given in the text. The SPW is electromagnetic (EM) when $n_y \gg n_z$ and is electrostatic (ES) when $n_z \gg n_y$.

Fig. 3 (Color online) AORSA-2D calculation of fast wave propagation for DIII-D-like parameters given in the text. The k_y spectrum of the binormal component E_β of the wave electric field in the Stix frame is shown for (a) a high-single-pass and (b) a low-single-pass case. Also, the contours of E_β are plotted for (c) a high single pass and (d) a low single pass case. Here, $E_\beta = \hat{\mathbf{e}}_\beta \cdot \mathbf{E} = (\mathbf{b} \times \hat{\mathbf{e}}_\alpha) \cdot \mathbf{E}$ where $\hat{\mathbf{e}}_\alpha$ is the part of the unit vector $\hat{\mathbf{e}}_x$ perpendicular to B with $x = R - R_0$.

Fig. 4 Plot of the difference function $D(\Delta)$ defined in the text vs the sheath width. The equation $D = 0$ for the self-consistent sheath potential has three roots

Fig. 5 (Color online) The self-consistent sheath potential vs index of refraction n_y including the effect of the sheath-plasma-wave (SPW) resonance for the parameters given in the text. Note the presence of multiple roots due to the SPW resonance. The root structure is shown in color in the online version.

Fig. 6 (Color online) The self-consistent sheath potential vs the magnetic field mismatch parameter B_x/B showing the multiple root structure. The sheath plasma wave resonance gives larger sheath potentials as B_x/B increases.

Fig. 7 (Color online) Fig. 7 (Color online) The self-consistent sheath potential vs density including the effect of the sheath-plasma-wave resonance for the parameters $n_y = 30$, $n_z = 6$, $B_x/B = 0.2$. The curve is shown for $E_0 = 10$ and 20 V/cm, where E_0 is the amplitude of the incident fast wave at the sheath-plasma interface defined in Eq. (7). Again there are multiple roots because of the nonlinear SPW resonance. The three branches are labeled by different colors in the online version.

Fig. 8 Plot of the fast wave electric field component E_y vs major radius R for the low single-pass case discussed in the text. Here, both $\text{Re}[E_y]$ (solid curve) and $\text{Im}[E_y]$ (dashed curve) are shown; the coordinate y is in the poloidal direction in the lab frame. The antenna is located on the far right, and the wall where the BC is applied is at the left end of the plot at $R = 0.95$ m, which corresponds to $x = 0$ in the WS model. Note the standing wave character of the field because of the poor central absorption.

Fig. A1 Sample solution showing $|\phi_n|/\Phi$ vs n for the parameters $\alpha = 0.2$, $k_0 = 0.25$, $K_y = 0.1$, $x_w = 1$, $k_w = 10$. The incoming wave at $n = 0$ is reflected and spread into many sidebands when the Bessel arguments are order unity.

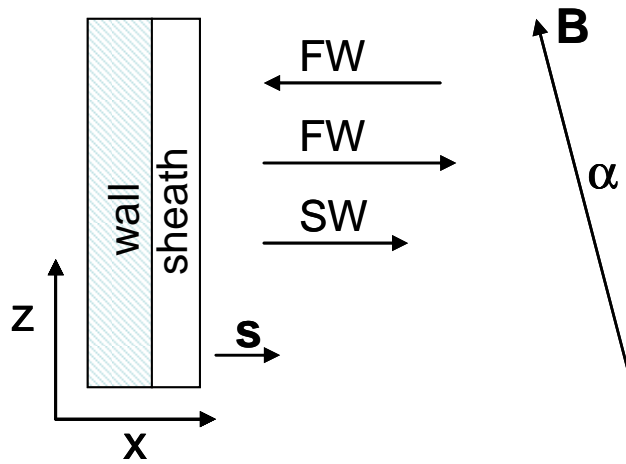


Fig. 1 Geometry of the scattering problem. An incoming fast wave (FW) generates a reflected FW and slow wave (SW) in order to satisfy the BC at the wall. The wave-coupling occurs when the B field has a projection normal to the wall ($\mathbf{s} \cdot \mathbf{b} \neq 0 \Rightarrow \alpha \neq 0$)

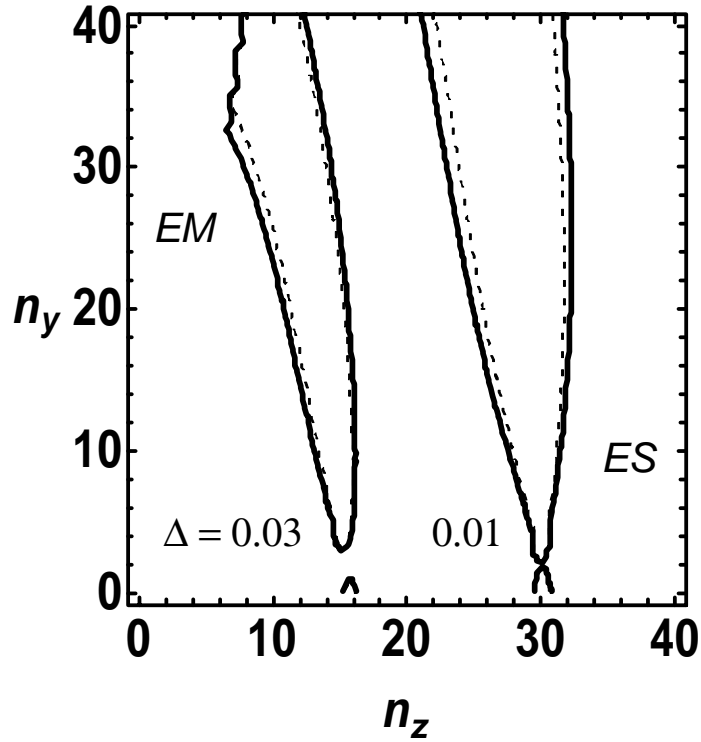


Fig. 2 Contour plot of the normalized SW amplitude, $|E_2/E_0|$, to illustrate the Sheath Plasma Wave (SPW) enhancement of the coupled waves. Shown are the contours $|E_2/E_0| = 5$ (solid line) and 6 (dashed line) for two values of the sheath width, $\Delta = 0.01$ and 0.03 cm, (not self consistent). The other parameters are given in the text. The SPW is electromagnetic (EM) when $n_y \gg n_z$ and is electrostatic (ES) when $n_z \gg n_y$.

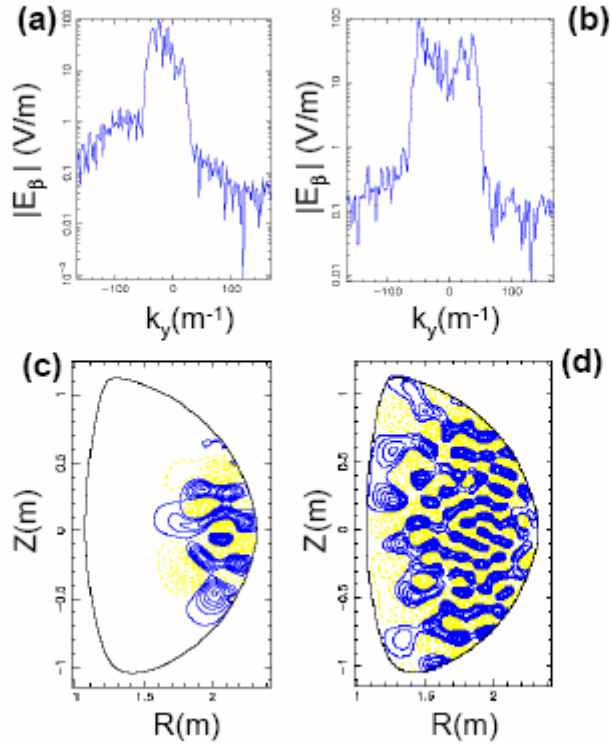


Fig. 3 (Color online) AORSA-2D calculation of fast wave propagation for DIII-D-like parameters given in the text. The k_y spectrum of the binormal component E_β of the wave electric field in the Stix frame is shown for (a) a high-single-pass and (b) a low-single-pass case. Also, the contours of E_β are plotted for (c) a high single pass and (d) a low single pass case. Here, $E_\beta = \hat{e}_\beta \cdot \mathbf{E} = (\mathbf{b} \times \hat{e}_\alpha) \cdot \mathbf{E}$ where \hat{e}_α is the part of the unit vector \hat{e}_x perpendicular to \mathbf{B} with $x = R - R_0$.

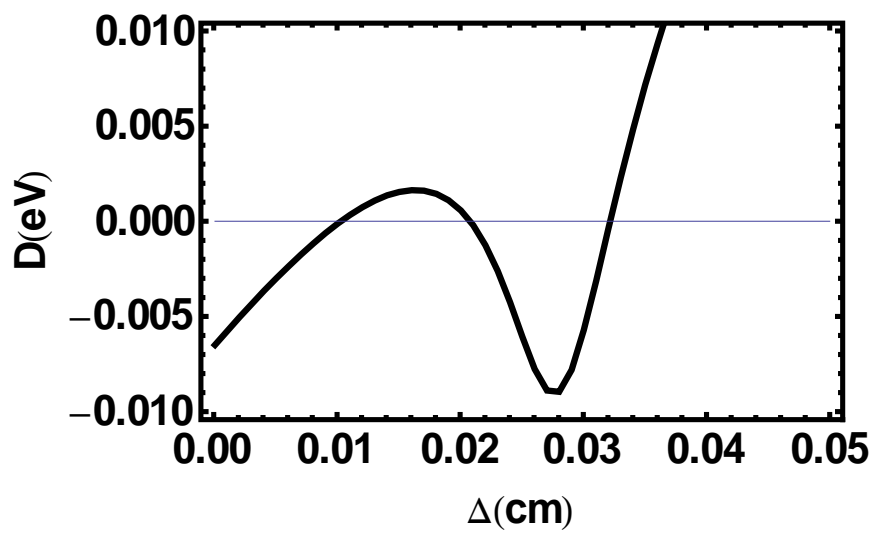


Fig. 4 Plot of the difference function $D(\Delta)$ defined in the text vs the sheath width. The equation $D = 0$ for the self-consistent sheath potential has three roots.

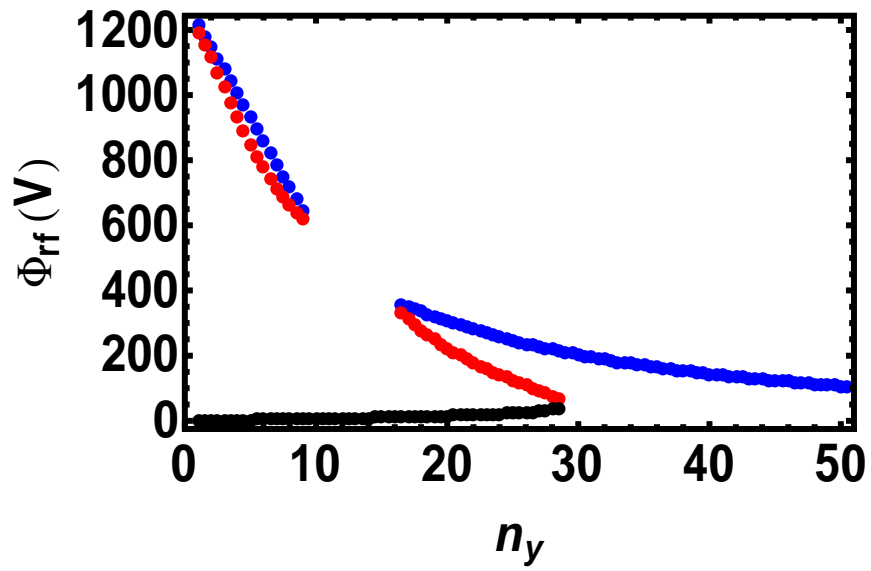


Fig. 5 (Color online) The self-consistent sheath potential vs index of refraction n_y including the effect of the sheath-plasma-wave (SPW) resonance for the parameters given in the text. Note the presence of multiple roots due to the SPW resonance. The root structure is shown in color in the online version.

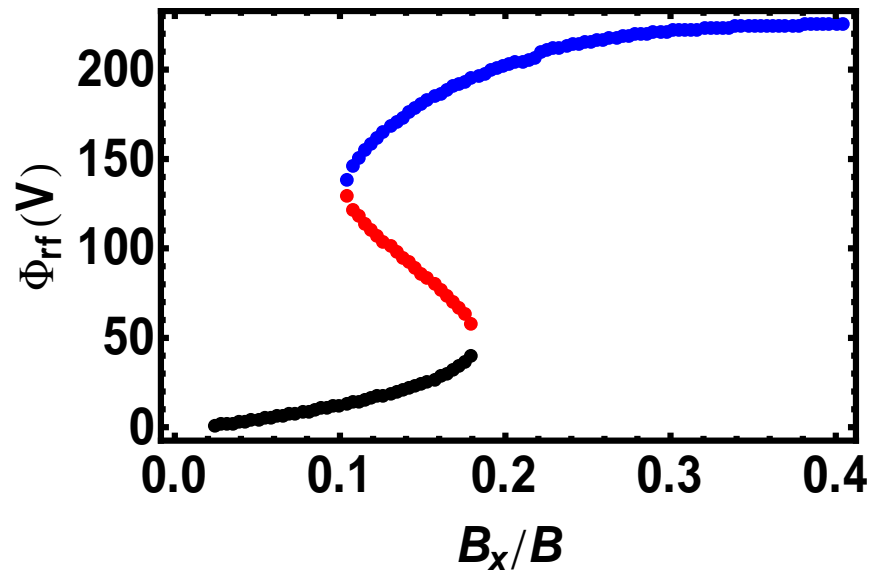


Fig. 6 (Color online) The self-consistent sheath potential vs the magnetic field mismatch parameter B_x/B showing the multiple root structure. The sheath plasma wave resonance gives larger sheath potentials as B_x/B increases.

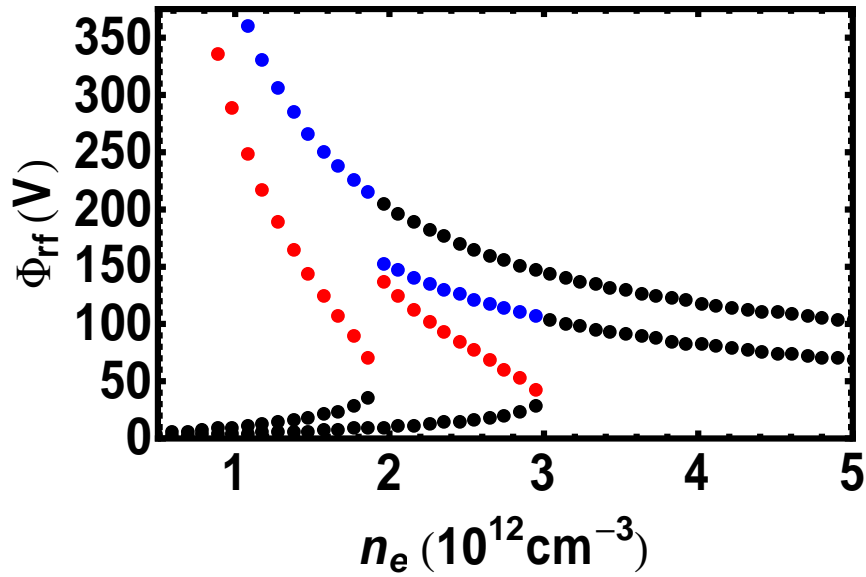


Fig. 7 (Color online) The self-consistent sheath potential vs density including the effect of the sheath-plasma-wave resonance for the parameters $n_y = 30$, $n_z = 6$, $B_x/B = 0.2$. The curve is shown for $E_0 = 10$ and 20 V/cm, where E_0 is the amplitude of the incident fast wave at the sheath-plasma interface defined in Eq. (7). Again there are multiple roots because of the nonlinear SPW resonance. The three branches are labeled by different colors in the online version.

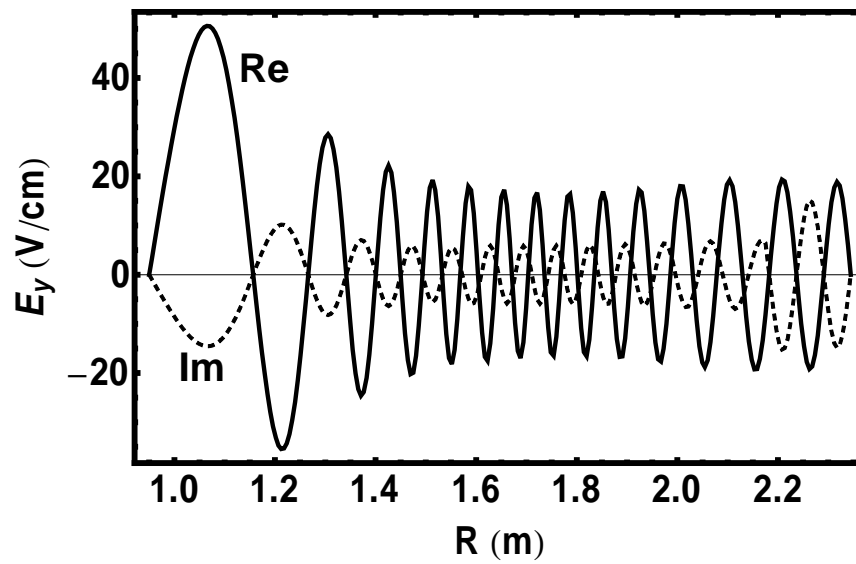


Fig. 8 Plot of the fast wave electric field component E_y vs major radius R for the low single-pass case discussed in the text. Here, both $\text{Re}[E_y]$ (solid curve) and $\text{Im}[E_y]$ (dashed curve) are shown; the coordinate y is in the poloidal direction in the lab frame. The antenna is located on the far right, and the wall where the BC is applied is at the left end of the plot at $R = 0.95$ m, which corresponds to $x = 0$ in the WS model. Note the standing wave character of the field because of the poor central absorption.

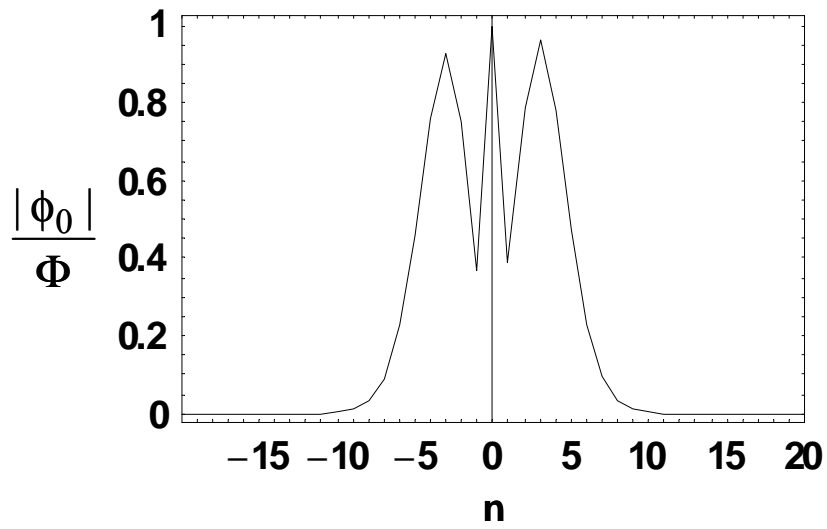


Fig. A1 Sample solution showing $|\phi_n|/\Phi$ vs n for the parameters $\alpha = 0.2$, $k_0 = 0.25$, $K_y = 0.1$, $x_w = 1$, $k_w = 10$. The incoming wave at $n = 0$ is reflected and spread into many sidebands when the Bessel arguments are order unity.